ADVANCED ELECTRONIC MATERIALS Open Access
www.advelectronicmat.de

Achieving High Ferroelectric Polarization in Ultrathin $BaTiO_3$ Films on Si

Pratik Bagul, Han Han, Pieter Lagrain, Stefanie Sergeant, Ilse Hoflijk, Jill Serron, Olivier Richard, Thierry Conard, Jan Van Houdt, Ingrid De Wolf, and Sean R. C. McMitchell**

Ferroelectrics show promise for low-power, non-volatile memory technologies. However, material challenges in state-of-the-art ferroelectric hafnates and the high coercive fields required limit their application in devices. Scaling of other candidate materials is challenging, often requiring epitaxial single-crystalline growth using specialised substrates. Here, ferroelectricity is demonstrated in polycrystalline $BaTiO_3$ films at 10 nm thickness on Si substrates. They exhibit the highest reported remnant polarization for polycrystalline layers, 13 µC cm^{-2}, a value that is competitive with the epitaxial $BaTiO_3$ state-of-the-art. This is realised by introducing a novel conductive oxygen barrier, platinum silicide, which also offers strain enhancement of the ferroelectricity. Moreover, it is demonstrated that these layers can be positioned in device-like stacks whilst maintaining ferroelectricity at 10 nm. The findings of polycrystalline perovskite ferroelectric growth in stack configurations akin to those in production flows paves the way for high performance perovskites with greater material complexity.

1. Introduction

Ferroelectric materials have attracted a lot of attention for their potential applications, such as memory technologies,[1–8] sensors and actuators,[9,10] energy harvesting,[11,12] electro-optics,[13–16] and medical imaging.[17] Ferroelectrics exhibit a spontaneous polarization below the Curie temperature, T_c, and are switchable by an electric field, which makes them ideal for low-power memory applications. Inserting a ferroelectric capacitor in a one transistor one capacitor (1T1C) memory element would yield a potential dynamic random-access memory (DRAM) replacement technology where the non-volatile nature significantly reduces operational power.[18] The remnant polarization (P_r) of the ferroelectric is a crucial figure of merit as it directly influences the transistor state and signal magnitude. Additionally, the coercive field (E_c) is another important material parameter, which, when low, enables low-voltage switching for low-power operation. Complex oxide perovskite ferroelectrics would be ideal materials because they offer a much lower E_c compared to competing materials, such as hafnate fluorites[19,20] and the relatively new wurtzite ferroelectrics,[21,22] while typically exhibiting high P_r. Until now, the lack of a practical process flow, scalable to suitable thickness dimensions (<15 nm), has significantly limited the application of these materials. In recent years, the observed ferroelectricity in epitaxial films with a thickness much lower than what was previously believed possible has renewed interest in perovskite ferroelectrics. Ferroelectricity has been reported in ultrathin epitaxial films of one such material, barium titanate ($BaTiO_3$), down to 2 nm.[7,23–28] However, the epitaxial growth of high-quality ferroelectric perovskites requires the use of specialized substrates such as $SrTiO_3$, $DyScO_3$, MgO, and YSZ, which are expensive and complex to integrate onto the Si wafers required for standard complementary metal-oxide-semiconductor (CMOS) fabrication processes. Incorporating these layers into Si-based devices often requires the use of difficult epitaxial tricks that need constant in-situ monitoring and only work directly on the Si wafer surface. Both conditions preclude the use of production-worthy 1T1C-type architectures where capacitors are inherently placed away from the Si wafer in terms of stack position. The use of polycrystalline ferroelectrics with production-compatible electrode templates can open new avenues for the practical integration of these materials in CMOS

P. Bagul, I. De Wolf
Department of Materials Engineering
KU Leuven
Kasteelpark Arenberg, Leuven 3001, Belgium
E-mail: pratik.bagul@imec.be

P. Bagul, H. Han, P. Lagrain, S. Sergeant, I. Hoflijk, J. Serron, O. Richard, T. Conard, J. Van Houdt, I. De Wolf, S. R. C. McMitchell
Imec
Kapeldreef 75, Leuven 3001, Belgium
E-mail: sean.mcmitchell@imec.be

J. Van Houdt
Department of Physics and Astronomy
KU Leuven
Celestijnenlaan, Leuven 3001, Belgium

The ORCID identification number(s) for the author(s) of this article can be found under https://doi.org/10.1002/aelm.202400440

DOI: 10.1002/aelm.202400440

technology. However, scaling has yet to be demonstrated in polycrystalline films, due to material- and processing-related challenges with perovskite ferroelectrics. Furthermore, the remanent polarization reported in polycrystalline ferroelectrics is typically only a fraction of their epitaxial counterparts, although in theory, large polarization should be achievable by engineering strain on ferroelectric perovskites using templates.

In this study, we report a novel strategy to scale polycrystalline $BaTiO_3$ films to an ultrathin thickness of 10 nm by using a platinum silicide template while achieving a high remanent polarization of 13 μC cm^{-2} (Pr of bulk $BaTiO_3$ is ≈26 μC cm^{-2}). This is higher than all values reported in the literature on polycrystalline and is competitive with epitaxial $BaTiO_3$ at these thicknesses. These high performance, ultra-thin films are grown by pulsed laser deposition, a technique once thought to be solely a research tool, but now is becoming increasingly industrially relevant with large area deposition tools readily available.[29] In addition, we demonstrate the potential of using this strategy to enable the application of perovskite ferroelectrics for memory applications in a CMOS-compatible process.

2. Results and Discussion

2.1. State-Of-The-Art Platinum Silicide

For the successful growth of ferroelectric $BaTiO_3$ on a Si-based stack, it is essential to have a bottom electrode layer that acts as an oxygen barrier to prevent the oxidation of the underlying layers. Silicon is particularly easy to oxidize under the deposition conditions needed for high-quality perovskite growth. Furthermore, the bottom electrode should also provide a template for the perovskite structure to encourage crystallinity. To meet these requirements in this stack type, we are the first to utilize the novel conductive oxygen barrier electrode material, platinum silicide. Platinum silicide has a similar conductivity as Pt and has been studied extensively for interconnects given its low formation temperatures, good conductivity, and relatively good thermal and chemical stability.[30–34] It has also been shown that epitaxial PtSi on (111) Si can improve the orientation of $LiTaO_3$ and thereby its ferroelectric properties.[35] However, in this study it was, for the first time, developed as a conductive oxygen barrier template layer for the growth of polycrystalline perovskites.

To be compatible with CMOS-based technology, the growth of the needed layers should be indiscriminate to stack position. By demonstrating performance of the platinum silicide-based capacitor stack grown on a commonly used polycrystalline electrode layer, TiN, deposited on a Si substrate, we illustrate the potential to meet this requirement. This stack configuration emulates a capacitor in the back-end-of-line (BEOL), however, it is important to note that the temperatures used in this work are much higher than the thermal budget of back-end-of-line processing. Here we deposited 10 nm Si and 10 nm Pt sequentially on the TiN layer using a direct-current (DC) sputtering process (see details in the Experimental Section). **Figure 1b** shows this as-deposited stack heterostructure along with the changes in the deposited stack after 750 °C annealing, and the stack with subsequent deposition of $LaNiO_3$ and $BaTiO_3$ are shown in Figure 1a and Figure 1c respectively. The formation of platinum silicide was studied using temperature-dependent in-situ x-ray diffraction measurements (XRD) from room temperature to 800 °C, which revealed the formation of a silicide phase at ≈230 °C, as shown in Figure S1 (Supporting Information). The metallic platinum peak (2θ≈39°) disappeared and a new peak (2θ≈56°) appeared, which can be attributed to the formation of platinum silicide (Pt_2Si). No further change was seen until 780 °C, which was higher than the temperature window of interest for our work. At higher temperatures, we observed multiple peaks likely related to the decomposition of TiN and the formation of oxides. However, this was not studied in detail. Silicide formation occurs by interdiffusion between Pt and Si, which has also been previously observed from other studies, and the formation temperature of this phase is in line with the reported literature.[36,37] Further confirmation of the formation of Pt_2Si was obtained using x- ray photoelectron spectroscopy (XPS) (Figure 1d), which showed a small shift in binding energy (≈1.1 eV) for Pt4f spectra compared to the reference with metallic platinum. This shift in binding energy corresponded to Pt_2Si,[33,38,39] and was in agreement with the XRD pattern. Furthermore, high-resolution transmission electron microscopy (TEM) images, as shown in Figure S2 (Supporting Information), also confirmed the intermixing of Pt and Si to form a silicide layer.

To verify the oxygen barrier properties of the platinum silicide, $BaTiO_3$ films with a 10 nm $LaNiO_3$ bottom electrode were grown on two different stack configurations, namely stack A (Pt/TiN/Si substrate) and stack B (Pt/Si/TiN/Si substrate). Delamination of the films was seen in stack A, as seen by scanning electron microscopy (SEM; Figure S3, Supporting Information). DC-sputtered Pt films are reported to have a less dense microstructure and smaller grain size thereby reducing the activation energy for oxygen interdiffusion,[40] agreeing well with the observation of stack A. It is likely that the grain boundary density was high in the deposited Pt providing migration paths for oxygen during the deposition process at elevated temperatures, thereby oxidizing the underlying layers. With the presence of silicon in stack B, the formation of platinum silicide through the interdiffusion of Si and Pt was expected. This resulted in a reduction in the observed grain boundary density preventing oxygen diffusion to the underlying layers and thus acting as an oxygen barrier layer. The XRD pattern for $BaTiO_3$ deposited on stack B confirmed the formation of Pt_2Si as shown in Figure 1e. Furthermore, we also noted that the Pt and Si layers intermixed during the high temperature deposition of $LaNiO_3$ (500 °C) followed by $BaTiO_3$ (750 °C) to form platinum silicide without ex-situ preanneal. The 40 nm $BaTiO_3$ film grown in this stack exhibited polycrystallinity with the presence of both (001) and (110) orientations. Ferroelectric positive-up-negative-down (PUND) measurements (Figure 1f) on this $BaTiO_3$ film show ferroelectricity with a high remanent polarization value ($2P_r$) of 38 μC cm^{-2}. This clearly shows that platinum silicide can enhance the ferroelectric properties of $BaTiO_3$ films in addition to its oxygen barrier properties.

2.2. Platinum Silicide on Si

To study the influence of platinum silicide on the $BaTiO_3$ films, a simplified stack consisting of 5 nm platinum deposited directly on a silicon wafer (**Figure 2a**). This was done to reduce stack

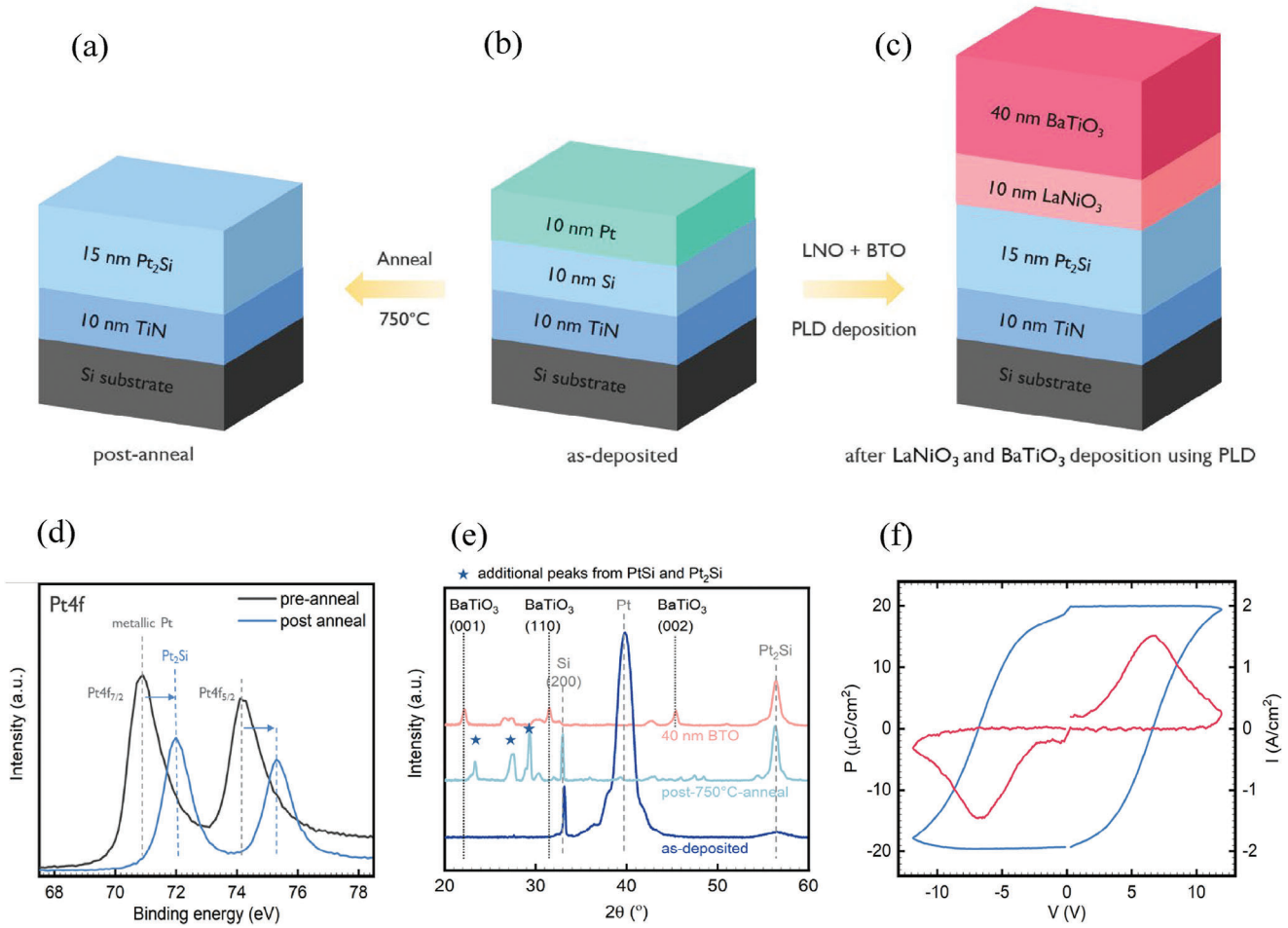

Figure 1. Template development for the high temperature deposition of perovskites Schematic of stack heterostructure of (a) post-750°C anneal resulting in the intermixing of Pt and Si to form platinum silicide, (b) as-deposited 10 nm Pt/10 nm Si/10 nm TiN/ 10 nm Si, and (c) after deposition of 40 nm $BaTiO_3$/10 nm $LaNiO_3$ using pulsed laser deposition (PLD) (d) X-ray photoelectron spectra for the as-deposited and post-750°C anneal heterostructure, (e) θ-2θ XRD pattern of the as-deposited, post-750°C anneal, and 40 nm $BaTiO_3$/10 nm $LaNiO_3$ films (f) P-V and *I*–*V* characteristics measured for the 40 nm $BaTiO_3$ films using positive-up-negative-down (PUND) measurements confirming ferroelectricity in the films.

complexity allowing for easier probing of intrinsic ferroelectric effects. XRD measurements were performed before and after annealing at 750 °C in vacuum to confirm phase formation and transformations in this stack. Figure 2d shows that the metallic Pt peak ($2\theta \approx 39.6°$) disappears, coinciding with the emergence of a new peak at $2\theta \approx 43.7°$, which could be attributed to the formation of a platinum silicide phase, PtSi. The one-to-one stoichiometry was likely the result of complete intermixing of Pt and Si due to the unlimited supply of crystalline Si, and thinner Pt. This is commonly observed when Pt is deposited directly on silicon wafers and then annealed.[30,36]

To confirm the identified phase from XRD, XPS measurements were undertaken on samples before and after annealing. The evolution of the Pt4f spectra is presented in Figure 2e. In the pre-annealed substrate, the $Pt4f_{7/2}$ peak was positioned at ≈70.9 eV which corresponds to metallic Pt. Upon annealing, a shift was observed in the $Pt4f_{7/2}$ binding energy to 72.4 eV. This is a known transition in the formation of PtSi.[33,38] Further confirmation of the PtSi phase was obtained using Raman spectroscopy (Figure 2f). The annealed substrate showed sharp Raman peaks at 82 cm^{-1} and 140 cm^{-1} which is consistent with previous studies on PtSi using Raman spectroscopy.[41] Pt_2Si is reported to have a weak Raman peak at 90cm^{-1} which was not detected, suggesting the absence of Pt_2Si. High-resolution TEM images of the silicide layer (Figure 2c) show grains extended from the bottom interface (with Si) to the top of the layer. In addition, moiré patterns were also observed suggesting the overlap of grains with multiple orientations. PtSi is commonly reported to follow the epitaxial orientation with (111) Si.[42–44] In contrast, here, the fast Fourier transform (FFT) images from this silicide layer showed that PtSi was polycrystalline. There was no epitaxial relationship observed with respect to the substrate, possibly due to the (001)-orientation of the Si. This is a trait that is typical for BEOL layers, allowing knowledge gained from this simplified stack to be applied to real-life devices.

Depending on the stack configuration, the platinum silicide used in this work had a mixed phase, primarily constituted of PtSi and Pt_2Si. Due to the formation process, compositional gradients have been observed within the layer, with Pt-rich phases observed toward the top interface. However, while the two main

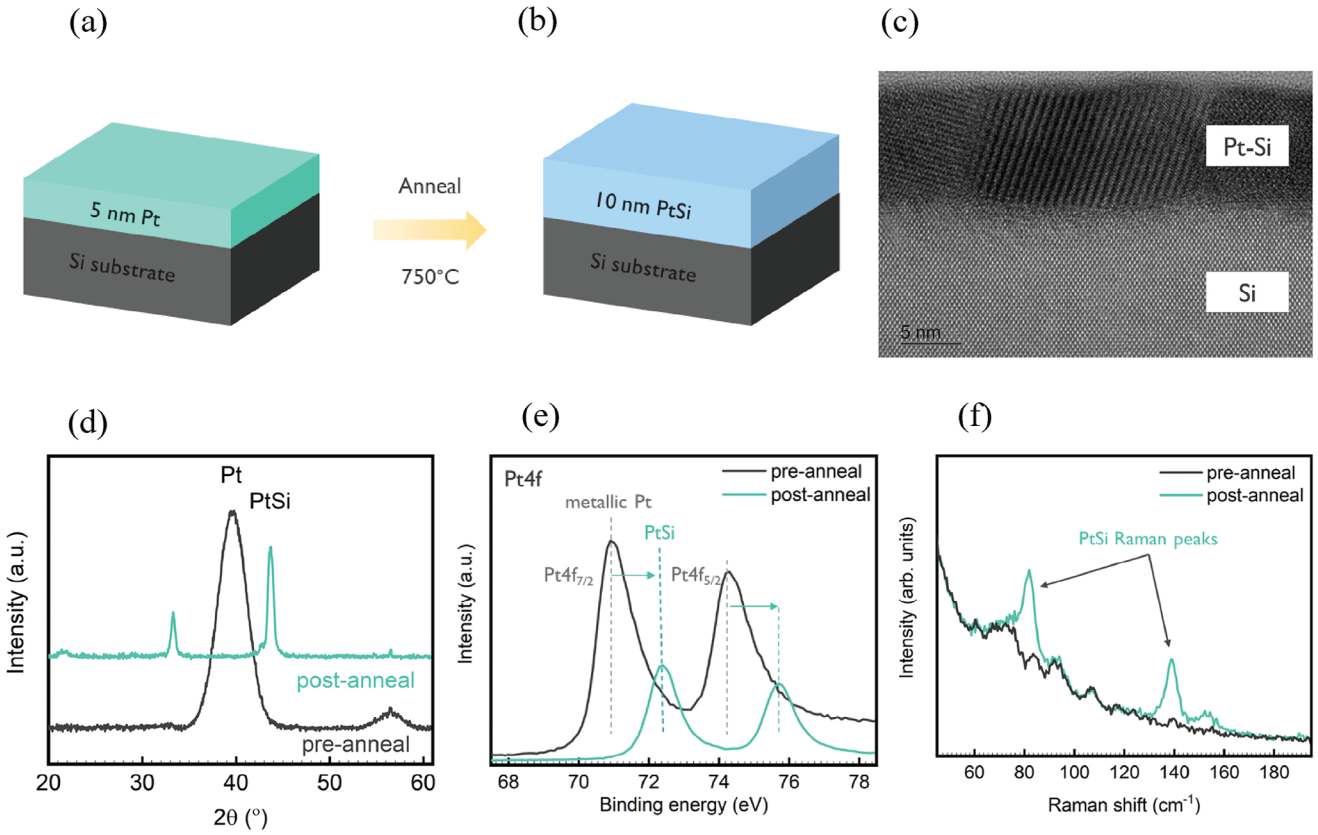

Figure 2. Platinum silicide formation on Si wafer (a) Stack heterostructure with 5 nm Pt deposited on Si wafer, (b) Platinum silicide formation after annealing the stack heterostructure at 750 °C, (c) High resolution TEM image showing the intermixing of platinum and silicon to form platinum silicide, (d) θ-2θ XRD pattern of the as-deposited heterostructure and post-750°C anneal, (e) XPS spectra of Pt4f showing the shift in the binding energy corresponding to the formation of platinum silicide (PtSi) after annealing at 750°C, and (f) Raman spectroscopy measurements confirming the formation of platinum silicide after annealing at 750°C from Raman peaks at 82 and 140 cm^{-1}.

phases, PtSi and Pt_2Si, have orthorhombic and tetragonal structures respectively, the unit cell sizes are similar leading to similar trends in strain. Furthermore, the conductivities of these phases are of the same order of magnitude as that of Pt, ensuring good electrode properties in both stack configurations. As such, there is no distinction made between the two phases in the following text.

2.3. Thickness Scaling of Polycrystalline $BaTiO_3$

Using the above simplified stack (5 nm Pt/Si substrate), the influence of thickness scaling of $BaTiO_3$ on its ferroelectric properties was investigated. $BaTiO_3$ films (10-35 nm) were grown via pulsed laser deposition (PLD) with 10 nm $LaNiO_3$ as the bottom electrode, as shown in the schematic in **Figure 3a**. The deposition conditions for both $BaTiO_3$ and $LaNiO_3$ are outlined in the methods section. The diffraction patterns collected in the $\theta-2\theta$ XRD scan geometry were measured for all $BaTiO_3$ and are shown in Figure 3b. The peaks seen at 21° and 32° indicated the presence of both (001) and (110) oriented grains. A noticeable shift toward higher 2θ angles with increasing film thickness was observed, suggesting a relaxation of the strain in the $BaTiO_3$ films. Furthermore, all films exhibit ferroelectric behavior as shown by PUND measurement results in Figure 3c. The remanent polarization (P_r) values were in the range of 13–18 μC cm^{-2}, which are higher than the polarization values previously reported for polycrystalline $BaTiO_3$. To put these remarkable polarization values in context, Figure 3d shows a comparison with the reported literature for $BaTiO_3$ films of varying thickness. Our $BaTiO_3$ films outperformed the limited studies on polycrystalline $BaTiO_3$ (square markers) and were comparable to epitaxial films (circular markers) at scaled thicknesses. PtSi seemed to enhance the ferroelectric response in the $BaTiO_3$ films, the presence of which was confirmed by the XRD peak at 43°. It is important to note that $BaTiO_3$ films grown on the more complex heterostructure stack (10 nm Pt/10 nm Si/10 nm TiN/Si) used to emulate growth in the back-end-of-line also exhibited ferroelectricity at 10 nm thickness (Figure S4, Supporting Information) showing that this work is transferable to real device structures.

2.4. Polarization Enhancement of Polycrystalline $BaTiO_3$

The cause of the significant enhancement of ferroelectricity by using a PtSi template for the perovskite stack is further investigated. Several studies have shown that ferroelectric polarization is influenced by factors such as strain, grain microstructure,

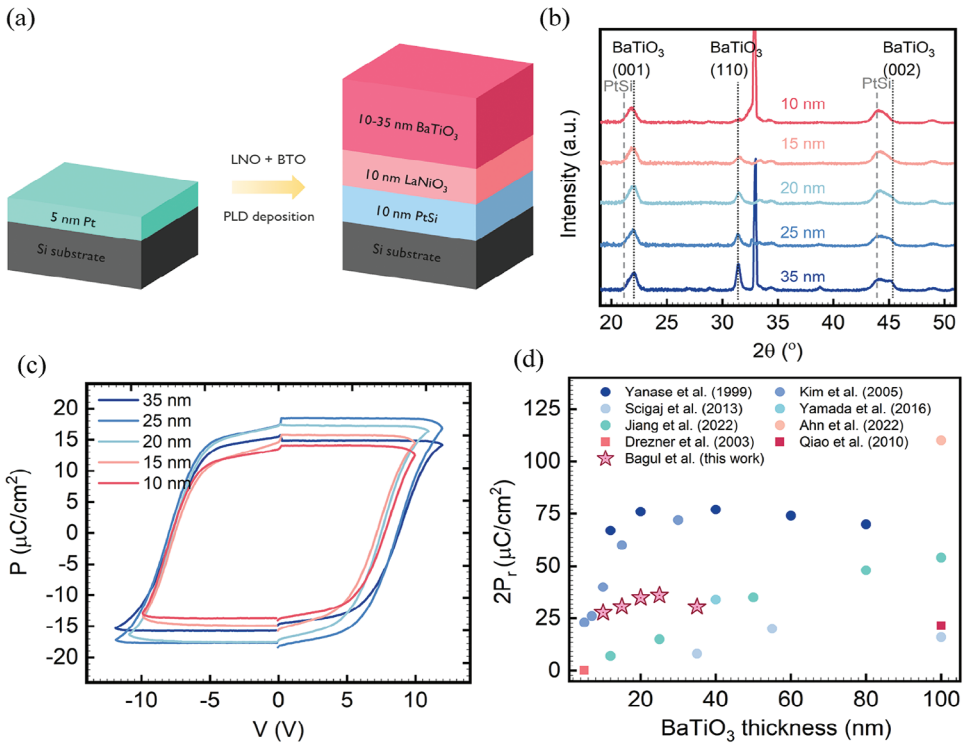

Figure 3. Thickness scaling of $BaTiO_3$ films on platinum silicide (a) schematic of the stack heterostructure (with 5 nm Pt/Si as starting stack) used for the depositions of 10 nm $LaNiO_3$ and $BaTiO_3$ films from 35 to 10 nm (b) X-ray diffraction pattern measured as a function of the $BaTiO_3$ film thickness. Polycrystalline films with a (001) and (110) $BaTiO_3$ orientation are observed, (c) *P–V* characteristics measured using PUND as a function of the $BaTiO_3$ film thickness, ferroelectricity observed in 10 nm polycrystalline $BaTiO_3$ films (d) Comparison of the ferroelectric remanent polarization of $BaTiO_3$ thin films with the previously reported literature. Square markers depict polycrystalline films, while circle markers depict epitaxial films.

oxygen vacancies, orientation of the film and crystal defects.[18,45,46,47] To understand the influence of these factors on our films, the remanent polarization (P_r), out-of-plane lattice parameter, and grain size for different films are plotted as a function of the $BaTiO_3$ thickness in **Figure 4**.

As $BaTiO_3$ was scaled down, the effects of different strain regimes could be seen. Changes in the out-of-plane lattice parameter are indicative of the in-plane strain. As the out-of-plane parameter expands, the in-plane parameter contracts in line with Poisson's ratio, and vice versa. In the thickest film (35 nm), the grain size and lattice parameter were like that of the strain-relaxed material, leading to a bulk-like P_r. As the film thickness reduced, the observed lattice parameter exhibited a small strain (≈0.25% out-of-plane with respect to the parameter at 35 nm thickness), while the grain size was still large. In this light strain regime (≈25 nm), the ferroelectric response was high (P_r = 18 μC cm^{-2} compared to P_r = 26 μC cm^{-2} of bulk $BaTiO_3$), clearly showing a strain enhancement of the ferroelectric response. It is well known that small strain can yield large responses in ferroelectrics,[48,49] and here, the observed ≈0.25% strain yielded a regime where interfacial strain enhanced ferroelectricity without inhibiting ionic displacement or grain growth. In the lower thickness range (10–20 nm), the out-of-plane lattice parameter increased with decreasing thickness, suggesting an increasing strain contribution. The ferroelectric response degraded in response to this; P_r decreased, while E_c increased. Furthermore, the grain size in this thickness range decreased in a stepwise fashion from the strain-relaxed regime and continued to reduce with decreasing film thickness. This suggests that a strain regime was present at these thicknesses that was dominated by interfaces. As the $BaTiO_3$ is further scaled from 20 nm, interfaces became more important leading to an increase in strain to ≈1% at 10 nm thickness. This magnitude of strain is known to have large effects on ferroelectricity,[50] and here led to a reduction of P_r to 13 μC cm^{-2} at 10 nm thickness as the interfacial strain inhibited ionic displacement. Below this thickness, no ferroelectricity was observed, probably because the interfacial strain became so large that ferroelectricity was inhibited. The strain values quoted here are all with respect to the 35 nm film and not to the bulk. The crystal structure within perovskite films is often distorted with respect to the bulk by microstructural phenomena. Thus, the most bulk-like thicker film was as the reference to account for this. This distortion likely enhanced ferroelectricity in these films to outperform other $BaTiO_3$ films reported in the literature. It is unlikely that the strain from $LaNiO_3$ alone was the only contributing factor to such high polarization values. The polarization values are typically much lower when $BaTiO_3$ is grown on the $LaNiO_3$ bottom electrode.[51–56] By a process of exclusion, PtSi must contribute to the strain imposed on the full perovskite stack and distort the $BaTiO_3$ structure in such a way to enhance the ferroelectric response. The observed change in coercive field with thickness of the films can also be explained by these same strain effects.[57–59] The trend in coercive field (extracted from piezoforce microscopy measurements (PFM)) with $BaTiO_3$ film thickness was like that of the lattice

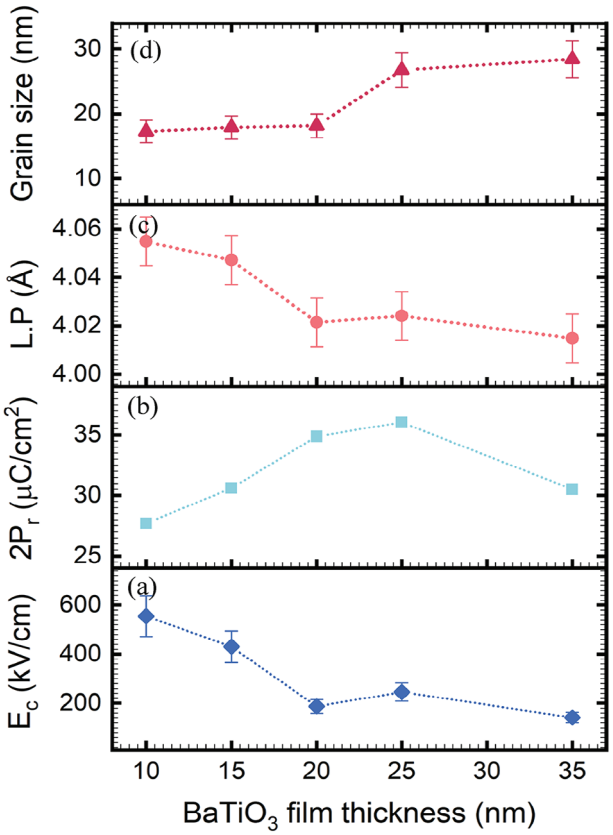

Figure 4. Figures of merit from different measurements as a function of $BaTiO_3$ films thickness a) Coercive field values extracted from CR-PFM measurements, b) Remanent polarization values extracted from PUND measurements, c) out-of-plane lattice parameter (LP) obtained from XRD scans, and d) grain size extracted from AFM scans.

parameters, further confirming the influence of strain on the perovskite stack. As interfacial strain became dominant at lower thickness, E_c increased, as P_r decreased. Ionic displacement was likely inhibited in this thickness regime, and a larger E-field was needed to switch the ferroelectric.

Furthermore, it is known that the strain state in a thin film can be influenced by the difference in the thermal expansion coefficients between the film and the underlying film/substrate. $LaNiO_3$ reportedly has a higher thermal expansion coefficient[60] than $BaTiO_3$, thus resulting in a compressive strain on the $BaTiO_3$ films during the post-deposition cooling process. A compressive strain would align the domains/polarization of the $BaTiO_3$ films along the applied electric field direction, contributing to the enhancement of ferroelectricity. Microstructural factors did not seem to have a dominant effect, yet they could have played a role in the modification of the ferroelectric response. Compared to reported literature on grain size dependence of polarization in $BaTiO_3$ films,[45,61] our films exhibited much smaller grain sizes. Nevertheless, they had high ferroelectric polarization values compared to literature. As described above, grain alignment is important and could contribute to an enhancement of polarization. Furthermore, an exceptionally high partial oxygen pressure was used during the growth of these films. Literature on the growth of $BaTiO_3$ films often report the use of low oxygen pressures to obtain the c-oriented tetragonal structures.[52,56,62,63] However, this generally leads to insufficient oxygenation during the growth process resulting in the formation of oxygen vacancies and causing high leakage and a degradation of the ferroelectric properties. On the other hand, the high partial oxygen pressures used in this study were chosen to reduce oxygen vacancies, reducing leakage, particularly at scaled thicknesses. Growth under these highly oxidizing conditions was only possible due to the use of the conductive oxygen barrier, PtSi. Whilst there are several factors that could be contributing to the enhancement in polarization as discussed, strain from the underlying layers was the dominant phenomenon, which can be seen from a clear dependence of the polarization on the change in the lattice parameter of the $BaTiO_3$ films.

2.5. Anomaly of the Coercive Field

One limitation of our $BaTiO_3$ films was the high switching voltage observed from ferroelectric hysteresis measurements. A comparison of the coercive field values extracted from hysteresis and contact resonance piezoresponse force microscopy (CR-PFM) measurements are shown in **Figure 5a**. A significant difference was seen between the switching fields obtained from the two measurements. Coercive field values of the order of 100 kV cm^{-1} have been previously reported for $BaTiO_3$ films in the literature.[25,26] The CR-PFM measurements revealed values on this order of magnitude; however, the hysteresis measurements yielded tenfold higher values. Such values are significantly higher than the known breakdown field for $BaTiO_3$,[64] suggesting the presence of parasitic/interfacial layers. These interfacial layers could store and remove the injected charge during one hysteresis cycle.[65] This would lead to an actual applied field across the $BaTiO_3$ layer which is much lower than that applied to the whole stack. Interfacial layers were, indeed, revealed as the additional layers between the Pt and $LaNiO_3$ layers in the TEM images (Figure 5b). The energy dispersive spectroscopy (EDS) spectra confirmed the presence of silicon oxide (SiO_2) and lanthanum oxide (La_2O_3) at the interface. These oxides SiO_2 ($k \approx 3.9$) and La_2O_3 ($k \approx 26$) have lower dielectric constant (k) values compared to $BaTiO_3$ ($k > 100$), and a lower-k value can indeed cause a higher voltage to drop across the layer. Therefore, an effective E_c for the device stack was measured to be much higher than the actual E_c of the ferroelectric $BaTiO_3$ layer, and even higher than the breakdown voltage of $BaTiO_3$ films ($E_{BD(BaTiO3)} \approx 1.5–3$ MV cm^{-1}).[64] The difference in the measured coercive field values can be explained by the fact that the field was saturated at the tip during the PFM measurements, making it more sensitive to local electromechanical displacements, thus mitigating the influence of the parasitic layers to an extent. In addition, the different measurement frequencies for the two techniques can also contribute to the observed differences. In general, higher measurement frequencies do not allow for complete domain switching, thus resulting in higher switching fields as observed with the PUND measurements ($f = 5$ kHz) compared to PFM measurements ($f = 1$ kHz). The inset in Figure 5a shows the amplitude and phase image from the PFM measurements on a 10 nm $BaTiO_3$ film (data for all $BaTiO_3$ films can be found in supplementary information). The amplitude contrast between

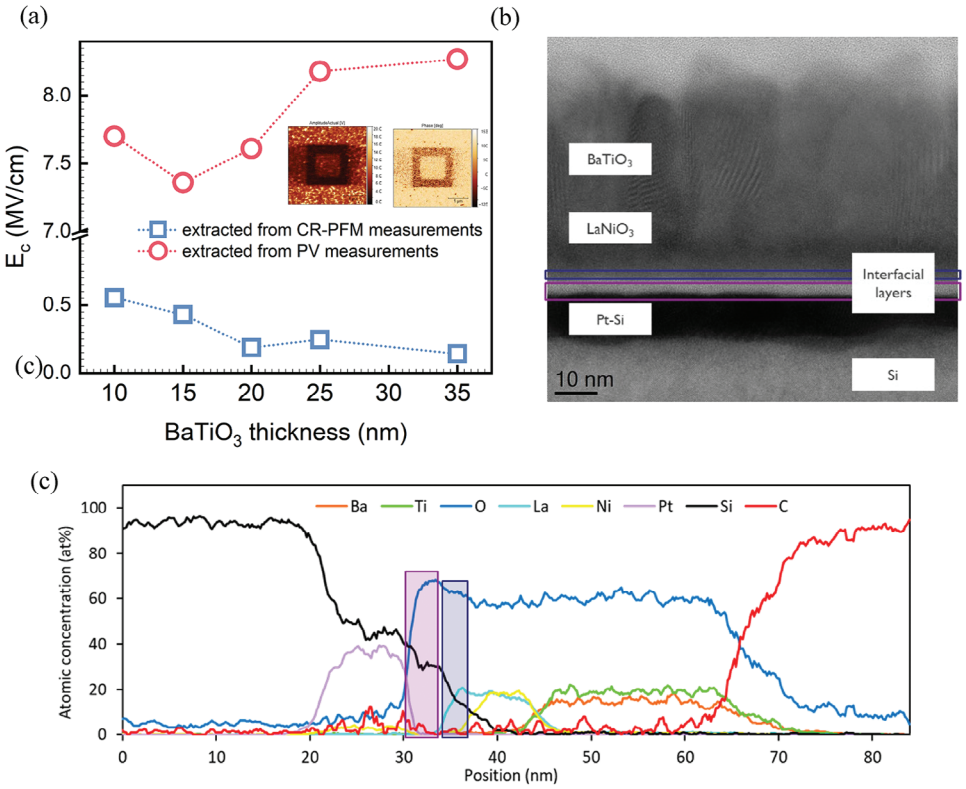

Figure 5. Understanding the influence of stack on coercive field of $BaTiO_3$ films a) Comparison of coercive field values obtained from PUND measurements and CR-PFM measurements for different $BaTiO_3$ film thicknesses, inset showing amplitude and phase image from PFM measurements on 10 nm $BaTiO_3$ films b) High-resolution TEM images showing the presence of interfacial layers between $LaNiO_3$ and PtSi, c) Energy dispersive spectra across this heterostructure, showing that the interfacial layers are comprised of SiO_2 and La_xO_y.

oppositely poled areas and absence of a perfect 180-degree phase contrast suggests the presence of charging effects in the films, which indicates non-ferroelectric contributions to the PFM signal in addition to the intrinsic ferroelectric response.[66,67] This makes it challenging to get an accurate quantitative understanding from the PFM measurements. Techniques have been reported separate the non-ferroelectric contributions for a better quantitative analysis,[68–70] however, it is not required here. In this work PFM data was simply used as a qualitative measure to provide a comparatively better estimate of the order of magnitude of the actual coercive field of $BaTiO_3$, and thus the qualitative conclusions are not affected by the presence of charging effects.

The formation of SiO_2 was likely due to the reaction between Si that migrated to the top of the PtSi layer and the oxygen in the PLD chamber during deposition. Although it is reported that Si segregation is observed at the top surface of the PtSi at elevated temperatures,[71] a compositional gradient was observed with a Pt-rich surface in our PtSi layers, which exerted an additional driving force for Si migration to the top surface and further oxidized before silicidation occurred. It is thought that the compositional gradient caused by intermixing of a Pt-Si bilayer would easily form the more energetically favourable Pt_2Si at the top interface leaving behind unreacted Si that would oxidize. At the same time, during the deposition of $LaNiO_3$, nickel ions impinging onto the surface of platinum silicide also reacted with the silicon from the PtSi. Nickel has a strong tendency to transition from the thermodynamically unstable Ni^{3+} valence state to Ni^{2+}.[72] The Ni ions toward the bottom surface of $LaNiO_3$ were in direct contact with the migrating Si and could form a silicide. The perovskite structure of $LaNiO_3$ commonly preserves stoichiometry and structure by pushing out outgrowths of the binary oxides, in this case La_2O_3. This migration of Ni into the PtSi layer and the formation of La_2O_3 was clearly detected from the EDS spectra (Figure 5c). Only nickel from the bottom 2–3 nm of $LaNiO_3$ migrated into the PtSi layer, suggesting that there were competing reactions between the formation of SiO_2 and nickel silicide. Once a certain thickness of SiO_2 was formed on top of PtSi, Ni could no longer migrate into PtSi to form nickel silicide. This was also confirmed by the EDS map where only a thin layer of SiO_2 was detected on top of PtSi with no other elements. Given the impact of oxygen on the formation of interfacial oxides layers and thereby on the coercive field, future work is needed to optimize the growth conditions in a way to achieve polarization enhancement while keeping the coercive field low.

3. Conclusion

In summary, we report a CMOS-compatible integration strategy for the growth of ultrathin ferroelectric $BaTiO_3$ films with platinum silicide as the bottom electrode. This platinum silicide layer enables the high-temperature growth of complex oxide perovskites by preventing the diffusion of oxygen to the

underlying layers. Furthermore, platinum silicide forms ≈ 250 °C, thus opening potential applications for back-end-of-line integration where the thermal budget is limited to 400 °C. The $BaTiO_3$ films grown on platinum silicide were polycrystalline and showed ferroelectric behavior down to 10 nm, which is the first time reported for polycrystalline films. Furthermore, high remanent polarization values were obtained at such scaled thicknesses, which was dominantly due to the strain on the $BaTiO_3$ films from the underlying layers. While the potential of platinum silicide in a state-of-the-art stack configuration was demonstrated, future optimization of the PtSi layer is still needed for true integration. The high effective E_c was shown to be due to parasitic oxide layers and thus should not diminish this first-time demonstration of a CMOS-compatible, thickness scaled polycrystalline perovskite ferroelectric capacitor with impressive properties. Nevertheless, it is an issue that must be solved and warrants further research. At the same time, the reliability of the electronic devices also needs to be studied in future work. Overall, even though the temperatures used in this work are significantly higher than the thermal budget for back-end-of-line processing, this work offers a new approach for the growth of polycrystalline perovskite ferroelectrics on Si substrates in device-like stacks. The learnings from this work can be transferred to other low-temperature perovskite ferroelectrics to achieve an industry-compatible integration process which is applicable to real-life devices.

4. Experimental Section

Thin Film Preparation: Pt and Pt/Si/TiN buffer layers were grown on two different 300 mm p-doped Si wafers using direct-current (DC) magnetron sputtering at room temperature, which were then diced into smaller pieces of 3.8 × 3.8 cm^2. $BaTiO_3$ films (10–40 nm) were grown on these smaller pieces using a Solmates 200 mm production Pulsed Laser Deposition system (KrF excimer laser). 10 nm $LaNiO_3$ films were used as a bottom electrode and were deposited in a single process with the $BaTiO_3$, using their respective stoichiometric ceramic target sources. $BaTiO_3$ films were grown at a temperature of 750 °C under an oxygen partial pressure of 0.20 mbar. With the incident laser beam rastering across the diameter of the rotating ceramic target, laser repetition rate of 20 Hz was used for a laser fluence of 1.0 J cm^{-2}. The number of laser pulses was calibrated for each deposition condition set to reach the desired thickness values which were evaluated using a Wollam RC2 spectroscopic ellipsometer (in the 400–900 nm wavelength range) and cross-section scanning electron microscopy (SEM). The deposition parameters for the 10 nm $LaNiO_3$ bottom electrode were kept the same for all samples, with a fluence of 1.5 J cm^{-2}, a substrate temperature of 500 °C, and an oxygen partial pressure of 0.10 mbar. The structural analysis of these films was then conducted using X-ray diffraction scans performed using a Panalytical X'Pert Pro diffractometer with a Cu Kα radiation source.

PtSi Characterization: To understand the formation of PtSi phases in the two different stacks, samples from each stack configuration were annealed at 750 °C. Raman spectroscopy was performed using the Horiba Jobin-Yvon HR800 Raman tool on the as-deposited and annealed samples from both stack configurations. Raman spectra were recorded in the 50–550 cm^{-1} wavenumber range with 405 and 532 nm wavelength laser radiation with a ND filter. XPS analysis was carried out using Angle Integrated mode using a QUANTES instrument from Physical Electronics with a monochromatized photon beam of 1486.6 eV. The spectra were analyzed using the CasaXPS software. In-situ X-ray diffraction (XRD) measurements were performed using the in-situ XRD setup at UGent. The samples were heated from room temperature to 1000 °C at a heating rate of 0.2 °C s^{-1} in a He atmosphere. XRD patterns were recorded throughout the annealing procedure with a fixed 2θ window of 20° around the PtSi peak of interest. θ–2θ scans in the range of 20–65° were also recorded before and after the anneal.

Transmission Electron Microscopy: Cross-sectional images of the sample structure were captured with a high-resolution transmission electron microscopy (HRTEM) using Titan G2 operated at 200 kV. Energy dispersive spectroscopy (EDS) was used along with HRTEM analysis to study the chemical composition of the stack.

Electrical Characterization: The evaluation of ferroelectric properties was carried out using MFM (metal-ferroelectric-metal) structures with Pt dots (90 µm in diameter) deposited as top electrodes using a shadow mask process. P-V hysteresis loops were measured by applying a triangular pulse with a frequency of 5 kHz using an aixACCT TF Analyzer 2000 measurement setup. Positive up negative down (PUND) measurements were performed using the same setup to extract the polarization values and switching voltage for all the samples. The non-switching response from the PUND measurements was subtracted from the switching response to obtain the absolute values of ferroelectric parameters without additional parasitic contributions. Both P-V and PUND measurements were carried out with a bias voltage in the range of 8–11 V. A frequency of 5 kHz and delay of 100 µs between read/write pulses was used for the PUND measurements.

Atomic Force and Piezoresponse Force Microscopy: The films were characterized using a Bruker IconPT AFM to access the morphology. The PFM measurements were carried out using Bruker Icon Dimension with an a.c. amplitude of 1 V and at a contact-resonance frequency of ≈105 kHz. The phase images were obtained after poling a box-in-a-box pattern with a bias of 8 V, where the total scan area was 4 µm, and the outer and the inner poled boxes were 2 and 1 µm, respectively. Butterfly curves were also obtained in contact-resonance PFM mode.

Supporting Information

Supporting Information is available from the Wiley Online Library or from the author.

Acknowledgements

The authors would like to thank Sofie Vandenbroucke (UGent) for the in-situ XRD measurements, and Danielle Verhaeren (IMEC) for the AFM measurements.

Conflict of Interest

The authors declare no conflict of interest.

Author Contributions

P.B. and S.R.C.M. designed the experiments. P.B. synthesized the thin films, carried out the structural characterization of the materials, and performed the ferroelectric measurements. H.H. and O.R. conducted HRTEM characterization. S.S carried out the Raman measurements, and I.H. and T.C. carried the XPS measurements. P.L and J.S. carried out the piezoresponse force microscopy measurements. P.B., S.R.C.M., and I.D.W. contributed to the analysis and understanding of data. P.B. and S.R.C.M. wrote the core of the manuscript. S.R.C.M, J.V.H and I.D.W. supervised the research. All authors contributed to the discussion and manuscript preparation and read the final manuscript.

Data Availability Statement

The data that support the findings of this study are available from the corresponding author upon reasonable request.

Keywords

barium titanate, ferroelectric memories, ferroelectrics, high remanent polarization, platinum silicide, pulsed laser deposition

Received: June 3, 2024
Revised: August 27, 2024
Published online: October 31, 2024

[1] J. F. Scott, *Science* **2007**, *315*, 954.
[2] J. F. Scott, in *Ferroelectric Random Access Memories: Fundamentals and Applications* (Eds: H. Ishiwara, M. Okuyama, Y. Arimoto), Springer Berlin Heidelberg, Berlin, Heidelberg **2004**, pp. 3–16.
[3] T. Mikolajick, U. Schroeder, S. Slesazeck, *IEEE Trans. Electron Devices* **2020**, *67*, 1434.
[4] A. Chanthbouala, A. Crassous, V. Garcia, K. Bouzehouane, S. Fusil, X. Moya, J. Allibe, B. Dlubak, J. Grollier, S. Xavier, C. Deranlot, A. Moshar, R. Proksch, N. D. Mathur, M. Bibes, A. Barthélémy, *Nat. Nanotech* **2012**, *7*, 101.
[5] Y. W. Yin, J. D. Burton, Y.-M. Kim, A. Y. Borisevich, S. J. Pennycook, S. M. Yang, T. W. Noh, A. Gruverman, X. G. Li, E. Y. Tsymbal, Q. Li, *Nat. Mater.* **2013**, *12*, 397.
[6] X. Long, H. Tan, F. Sánchez, I. Fina, J. Fontcuberta, *Nat. Commun.* **2021**, *12*, 382.
[7] V. Garcia, S. Fusil, K. Bouzehouane, S. Enouz-Vedrenne, N. D. Mathur, A. Barthélémy, M. Bibes, *Nature* **2009**, *460*, 81.
[8] M. Qian, I. Fina, F. Sánchez, J. Fontcuberta, *Small* **2019**, *15*, 1805042.
[9] C. B. Eom, S. Trolier-McKinstry, *MRS Bull.* **2012**, *37*, 1007.
[10] I. Kanno, *Jpn. J. Appl. Phys.* **2018**, *57*, 040101.
[11] H. Zhang, T. Wei, Q. Zhang, W. Ma, P. Fan, D. Salamon, S.-T. Zhang, B. Nan, H. Tan, Z.-G. Ye, *J. Mater. Chem. C* **2020**, *8*, 16648.
[12] L. Yang, X. Kong, F. Li, H. Hao, Z. Cheng, H. Liu, J.-F. Li, S. Zhang, *Prog. Mater. Sci.* **2019**, *102*, 72.
[13] A. Petraru, J. Schubert, M. Schmid, C.h. Buchal, *Appl. Phys. Lett.* **2002**, *81*, 1375.
[14] C. Xiong, W. H. P. Pernice, J. H. Ngai, J. W. Reiner, D. Kumah, F. J. Walker, C. H. Ahn, H. X. Tang, *Nano Lett.* **2014**, *14*, 1419.
[15] S. Abel, F. Eltes, J. E. Ortmann, A. Messner, P. Castera, T. Wagner, D. Urbonas, A. Rosa, A. M. Gutierrez, D. Tulli, P. Ma, B. Baeuerle, A. Josten, W. Heni, D. Caimi, L. Czornomaz, A. A. Demkov, J. Leuthold, P. Sanchis, J. Fompeyrine, *Nat. Mater.* **2019**, *18*, 42.
[16] B. W. Wessels, *Annu. Rev. Mater. Res.* **2007**, *37*, 659.
[17] W. Wang, J. Li, H. Liu, S. Ge, *Adv. Sci. (Weinh)* **2020**, *8*, 2003074.
[18] N. Setter, D. Damjanovic, L. Eng, G. Fox, S. Gevorgian, S. Hong, A. Kingon, H. Kohlstedt, N. Y. Park, G. B. Stephenson, I. Stolitchnov, A. K. Taganstev, D. V. Taylor, T. Yamada, S. Streiffer, *J. Appl. Phys.* **2006**, *100*, 051606.
[19] T. S. Böscke, J. Müller, D. Bräuhaus, U. Schröder, U. Böttger, *Appl. Phys. Lett.* **2011**, *99*, 102903.
[20] T. Mikolajick, S. Slesazeck, M. H. Park, U. Schroeder, *MRS Bull.* **2018**, *43*, 340.
[21] S. Fichtner, N. Wolff, F. Lofink, L. Kienle, B. Wagner, *J. Appl. Phys.* **2019**, *125*, 114103.
[22] S. R. C. McMitchell, A. M. Walke, K. Banerjee, S. Mertens, X. Piao, M. Mao, K. Katcko, G. Vellianitis, M. Van Dal, Y.-M. Lin, G. Van den Bosch, R. Delhougne, G. S. Kar, *ACS Appl. Electron. Mater.* **2023**, *5*, 858.
[23] N. Y. Naoko Yanase, K. A. Kazuhide Abe, N. F. Noburu Fukushima, T. K. Takashi Kawakubo, *Jpn. J. Appl. Phys.* **1999**, *38*, 5305.
[24] J. Junquera, P. Ghosez, *Nature* **2003**, *422*, 506.
[25] Y. S. Kim, D. H. Kim, J. D. Kim, Y. J. Chang, T. W. Noh, J. H. Kong, K. Char, Y. D. Park, S. D. Bu, J.-G. Yoon, J.-S. Chung, *Appl. Phys. Lett.* **2005**, *86*, 102907.
[26] Y. Jiang, E. Parsonnet, A. Qualls, W. Zhao, S. Susarla, D. Pesquera, A. Dasgupta, M. Acharya, H. Zhang, T. Gosavi, C.-C. Lin, D. E. Nikonov, H. Li, I. A. Young, R. Ramesh, L. W. Martin, *Nat. Mater.* **2022**, *21*, 779.
[27] D. D. Fong, G. B. Stephenson, S. K. Streiffer, J. A. Eastman, O. Auciello, P. H. Fuoss, C. Thompson, *Science* **2004**, *304*, 1650.
[28] E. Gradauskaite, Q. N. Meier, N. Gray, M. F. Sarott, T. Scharsach, M. Campanini, T. Moran, A. Vogel, K. Del Cid-Ledezma, B. D. Huey, M. D. Rossell, M. Fiebig, M. Trassin, *Nat. Mater.* **2023**, *22*, 1492.
[29] S. R. C. McMitchell, *APL Mater.* **2015**, *3*, 062301.
[30] J. C. Taylor, *J. Mater. Res.* **2021**, *36*, 211.
[31] S. P. Murarka, *Intermetallics* **1995**, *3*, 173.
[32] R. A. Donaton, S. Jin, H. Bender, M. Zagrebnov, K. Baert, K. Maex, A. Vantomme, G. Langouche, *MRS Online Proc. Libr.* **1998**, *514*, 241.
[33] R. T. Fryer, R. J. Lad, *J. Alloys Compd.* **2016**, *682*, 216.
[34] E. G. Colgan, J. P. Gambino, Q. Z. Hong, *Mater. Sci. Eng.: R: Rep.* **1996**, *16*, 43.
[35] Y. Tao, F. Gitmans, Z. Sitar, H. Pierhöfer, A. Kündig, I. Gamboni, P. Günter, *Ferroelectrics* **1997**, *201*, 245.
[36] E. Conforto, P. E. Schmid, *Philosop. Magazine A* **2001**, *81*, 61.
[37] K. V. Chizh, V. P. Dubkov, V. M. Senkov, I. V. Pirshin, L. V. Arapkina, S. A. Mironov, A. S. Orekhov, V. A. Yuryev, *J. Alloys Compd.* **2020**, *843*, 155908.
[38] G. Larrieu, E. Dubois, X. Wallart, X. Baie, J. Katcki, *J. Appl. Phys.* **2003**, *94*, 7801.
[39] K. Idczak, S. Owczarek, L. Markowski, *Appl. Surf. Sci.* **2022**, *572*, 151345.
[40] E.-S. Choi, S.-G. Yoon, W.-Y. Choi, H.-G. Kim, *Appl. Surf. Sci.* **1999**, *141*, 77.
[41] J. C. Tsang, R. Matz, Y. Yokota, G. W. Rubloff, *J. Vac. Sci. Technol. A* **1984**, *2*, 556.
[42] H. Kawarada, M. Ishida, J. Nakanishi, I. Ohdomari, S. Horiuchi, *Philosop. Magazine A* **1986**, *54*, 729.
[43] R. W. Fathauer, Q. F. Xiao, S. Hashimoto, C. W. Nieh, *Appl. Phys. Lett.* **1990**, *57*, 686.
[44] K. Konuma, H. Utsumi, *J. Appl. Phys.* **1994**, *76*, 2181.
[45] J. F. Ihlefeld, D. T. Harris, R. Keech, J. L. Jones, J. Maria, S. Trolier-McKinstry, *J. Am. Ceram. Soc.* **2016**, *99*, 2537.
[46] S. H. Park, J. Y. Kim, J. Y. Song, H. W. Jang, *Adv. Phys. Res.* **2023**, *2*, 2200096.
[47] L. W. Martin, A. M. Rappe, *Nat. Rev. Mater.* **2016**, *2*, 16087.
[48] D. G. Schlom, L.-Q. Chen, C.-B. Eom, K. M. Rabe, S. K. Streiffer, J.-M. Triscone, *Annu. Rev. Mater. Res.* **2007**, *37*, 589.
[49] A. R. Damodaran, J. C. Agar, S. Pandya, Z. Chen, L. Dedon, R. Xu, B. Apgar, S. Saremi, L. W. Martin, *J. Phys.: Condens. Matter* **2016**, *28*, 263001.
[50] R. Xu, J. Huang, E. S. Barnard, S. S. Hong, P. Singh, E. K. Wong, T. Jansen, V. Harbola, J. Xiao, B. Y. Wang, S. Crossley, D. Lu, S. Liu, H. Y. Hwang, *Nat. Commun.* **2020**, *11*, 3141.
[51] Y. Drezner, S. Berger, *J. Appl. Phys.* **2003**, *94*, 6774.
[52] L. Qiao, X. Bi, *Phys. Stat. Sol.* **2010**, *207*, 2511.
[53] L. Qiao, X. Bi, *J. Cryst. Growth* **2008**, *310*, 2780.
[54] L. Qiao, X. Bi, *Appl. Phys. Lett.* **2008**, *92*, 062912.
[55] L. Qiao, X. Bi, *J. Mater. Chem.* **2011**, *21*, 6280.
[56] M. Scigaj, C. H. Chao, J. Gázquez, I. Fina, R. Moalla, G. Saint-Girons, M. F. Chisholm, G. Herranz, J. Fontcuberta, R. Bachelet, F. Sánchez, *Appl. Phys. Lett.* **2016**, *109*, 122903.
[57] S. Choudhury, Y. L. Li, L. Q. Chen, Q. X. Jia, *Appl. Phys. Lett.* **2008**, *92*, 142907.
[58] M. D. Biegalski, D. H. Kim, S. Choudhury, L. Q. Chen, H. M. Christen, K. Dörr, *Appl. Phys. Lett.* **2011**, *98*, 142902.

[59] Y. Tong, M. Liu, H. M. Chen, G. P. Li, H. Fang, J. Wang, Z. Ma, *J. Appl. Phys.* **2015**, *117*, 074102.
[60] K. Murakoshi, K. Fukamachi, N. Sakamoto, T. Ohno, T. Kiguchi, T. Matsuda, T. Konno, N. Wakiya, H. Suzuki, *J. Ceram. Soc. Japan* **2013**, *121*, 273.
[61] Y. Tan, J. Zhang, Y. Wu, C. Wang, V. Koval, B. Shi, H. Ye, R. McKinnon, G. Viola, H. Yan, *Sci. Rep.* **2015**, *5*, 9953.
[62] J. Gong, M. Kawasaki, K. Fujito, U. Tanaka, N. Ishizawa, M. Yoshimoto, H. Koinuma, M. Kumagai, K. Hirai, K. Horiguchi, *Jpn. J. Appl. Phys.* **1993**, *32*, L687.
[63] J. Lyu, S. Estandía, J. Gazquez, M. F. Chisholm, I. Fina, N. Dix, J. Fontcuberta, F. Sánchez, *ACS Appl. Mater. Interfaces* **2018**, *10*, 25529.
[64] H. Wu, P. Ponath, E. L. Lin, R. M. Wallace, C. Young, J. G. Ekerdt, A. A. Demkov, M. R. McCartney, D. J. Smith, *J. Vac. Sci. Technol., B: Nanotechnol. Microelectron.: Mater., Process., Meas., Phenom.* **2020**, *38*, 044007.
[65] O. Trithaveesak, J. Schubert, C. Buchal, *J. Appl. Phys.* **2005**, *98*, 114101.
[66] D. Seol, B. Kim, Y. Kim, *Curr. Appl. Phys.* **2017**, *17*, 661.
[67] N. Balke, P. Maksymovych, S. Jesse, A. Herklotz, A. Tselev, C.-B. Eom, I. I. Kravchenko, P. Yu, S. V. Kalinin, *ACS Nano* **2015**, *9*, 6484.
[68] H. Tan, J. Lyu, Y. Sheng, P. Machado, T. Song, A. Bhatnagar, M. Coll, F. Sánchez, J. Fontcuberta, I. Fina, *Appl. Surf. Sci.* **2023**, *607*, 154991.
[69] N. Balke, S. Jesse, P. Yu, B. Carmichael, S. V. Kalinin, A. Tselev, *Nanotechnology* **2016**, *27*, 425707.
[70] A. Gomez, T. Puig, X. Obradors, *Appl. Surf. Sci.* **2018**, *439*, 577.
[71] R. Matz, R. J. Purtell, Y. Yokota, G. W. Rubloff, P. S. Ho, *J. Vac. Sci. Technol. A* **1984**, *2*, 253.
[72] L. Qiao, X. Bi, *Acta Mater.* **2009**, *57*, 4109.